

Regenerative water sources on surfaces of airless bodies

Cheng Zhu^{1,2}, Sándor Góbi^{1,2,6}, Matthew J. Abplanalp^{1,2}, Robert Frigge^{1,2}, Jeffrey J. Gillis-Davis^{3*}, Gerardo Dominguez⁴, Katarina Miljković⁵ and Ralf I. Kaiser^{1,2*}

Spectroscopic signatures of water and hydroxyl radicals have been observed on the surfaces of asteroids^{1–3}. As the lifetime of the exposed water ice is on the order of 10⁴ to 10⁶ yr in the inner asteroid belt⁴, there must be mechanisms to replenish the water in the absence of recent ice-exposing processes. However, such regenerative water-ice sources on asteroids are still elusive. Here we perform laboratory experiments by exposing the samples of the Murchison meteorite to energetic electrons and laser irradiation, simulating, respectively, the secondary electrons generated by the solar wind as well as galactic cosmic ray particles and the micrometeorites impacting on an asteroid. We find that a single simulated space-weathering component is insufficient and both are needed to regenerate water at low temperatures at the desired timescales. We propose that two main mechanisms can be the source of surface water on asteroids: low-temperature oxidation of organics and mineral dehydration.

We study the effect of space weathering on asteroid surficial water signatures by simulating the effect of cosmic rays and micrometeorites in laboratory conditions on a sample of the Murchison meteorite. Previous studies that used laser irradiation as a proxy of micrometeorite bombardment^{5,6} and 40 keV He⁺ and Ar⁺ ions to simulate solar wind irradiation⁷ observed only a final depletion of surface water and/or hydroxyl groups^{6–8}, leaving the question of the source of water signatures on asteroids open. To simulate space weathering, our experiments were conducted in an ultra-high vacuum (UHV) surface-science machine operated at a base pressure of a few 10^{–11} torr (a few 10^{–14} bar). Murchison meteorite powder was pressed onto a polished silver substrate and cooled in separate experiments to 5.5 ± 0.2 K and 150 ± 0.2 K, which represent the temperature limit allowed by our instrument and the characteristic equatorial temperature of asteroids⁹, respectively. The low temperature is comparable to the extreme temperatures in lunar permanently shadowed regions below 20 K, which may also exist on asteroids. These samples were irradiated: (1) by energetic electrons to simulate the cascade of secondary electrons generated by charged particles—primarily protons—from the solar wind and galactic cosmic rays while penetrating solids¹⁰; (2) by a pulsed infrared laser (see Methods) to create rapid thermal events with a maximum temperature exceeding diurnal temperatures, and similar to those experienced during micrometeorite impact events^{5,6,11}; and (3) both irradiation sources simultaneously (Supplementary Table 1). After the irradiation, the samples were heated at a rate of 1 K min^{–1}

to 300 K defined as temperature-programmed desorption (TPD). During the experiments, the mineral samples and the gas phases were monitored via in situ Fourier-transform infrared (FTIR) spectrometry and by an on-line quadrupole mass spectrometer (QMS), respectively (see Methods). FTIR and QMS data from irradiation experiments were compared with data for blank experiments to assess the generation of molecular species (see Methods).

Characteristic infrared absorptions of the Murchison meteorite connected to hydrated phyllosilicates—oxygen–hydrogen (O–H) stretches at 2.73 μm (3,660 cm^{–1}) and 2.94 μm (3,400 cm^{–1}) and silicon–oxygen (Si–O) stretches at 9.09 μm (1,100 cm^{–1}) and 9.90 μm (1,010 cm^{–1})—and organics—carbon–hydrogen (C–H) stretches at 3.38 μm (2,955 cm^{–1}), 3.42 μm (2,922 cm^{–1}) and 3.51 μm (2,848 cm^{–1})—were observed before the irradiation (Fig. 1)^{6,7}. Minor differences were observed in the infrared spectra of unirradiated samples due to meteorite heterogeneity. After the irradiation by electrons or by the laser, no remarkable changes were observed in the infrared spectra at 5 K and 150 K. Previous studies of single irradiation experiments on Murchison samples also identified unremarkable changes or an increase in organics^{6–8}.

Simultaneous irradiation with energetic electrons and the laser, however, led to the observable degradation of organics (at 5 K and 150 K) and phyllosilicates (at 150 K) as evident from the decline of absorptions of C–H stretches at 3.38 μm (2,955 cm^{–1}), 3.42 μm (2,922 cm^{–1}) and 3.51 μm (2,848 cm^{–1}), and the Si–O stretch at 9.90 μm (1,010 cm^{–1}) (Fig. 1). Simultaneously, strong absorptions emerged at 2.96 μm (3,380 cm^{–1}), 4.49 μm (2,225 cm^{–1}), 6.11 μm (1,637 cm^{–1}) and 4.27 μm (2,341 cm^{–1}), which can be assigned to the O–H stretch of water ($\nu_1/\nu_3(\text{H}_2\text{O})$), the silicon–hydrogen stretch ($\nu(\text{Si–H})$), the bending of water ($\nu_2(\text{H}_2\text{O})$), and the asymmetric stretch of carbon dioxide ($\nu_3(\text{CO}_2)$), respectively⁷. These effects are especially remarkable in the 150 K irradiation experiment. In particular, the ratio of the two new peaks at 2.96 and 6.11 μm agrees well with those of solid water-ice¹². Figure 2 depicts the temporal evolution of the integrated areas of organics as monitored via the decay of the C–H stretches at 3.38 μm (2,955 cm^{–1}), 3.42 μm (2,922 cm^{–1}) and 3.51 μm (2,848 cm^{–1}), and the formation of water and carbon dioxide during the irradiation. The decay of the C–H stretches of the organics and the concurrent growth of water and carbon dioxide were fit via first-order kinetics with rate constants of $(1.4 \pm 0.2) \times 10^{-4} \text{ s}^{-1}$, $(9.8 \pm 1.4) \times 10^{-4} \text{ s}^{-1}$ and $(2.0 \pm 0.5) \times 10^{-4} \text{ s}^{-1}$, respectively¹³. After the TPD, a small amount of residual water was observed in the infrared spectrum of the sample irradiated at 150 K.

¹Department of Chemistry, University of Hawai'i at Mānoa, Honolulu, HI, USA. ²W.M. Keck Laboratory in Astrochemistry, University of Hawai'i at Mānoa, Honolulu, HI, USA. ³Hawai'i Institute of Geophysics and Planetology, University of Hawai'i at Mānoa, Honolulu, HI, USA. ⁴Department of Physics, California State University San Marcos, San Marcos, CA, USA. ⁵School of Earth and Planetary Science, Space Science and Technology Centre, Curtin University, Perth, Western Australia, Australia. ⁶Present address: Department of Chemistry, University of Coimbra, Coimbra, Portugal. *e-mail: gillis@higp.hawaii.edu; ralfk@hawaii.edu

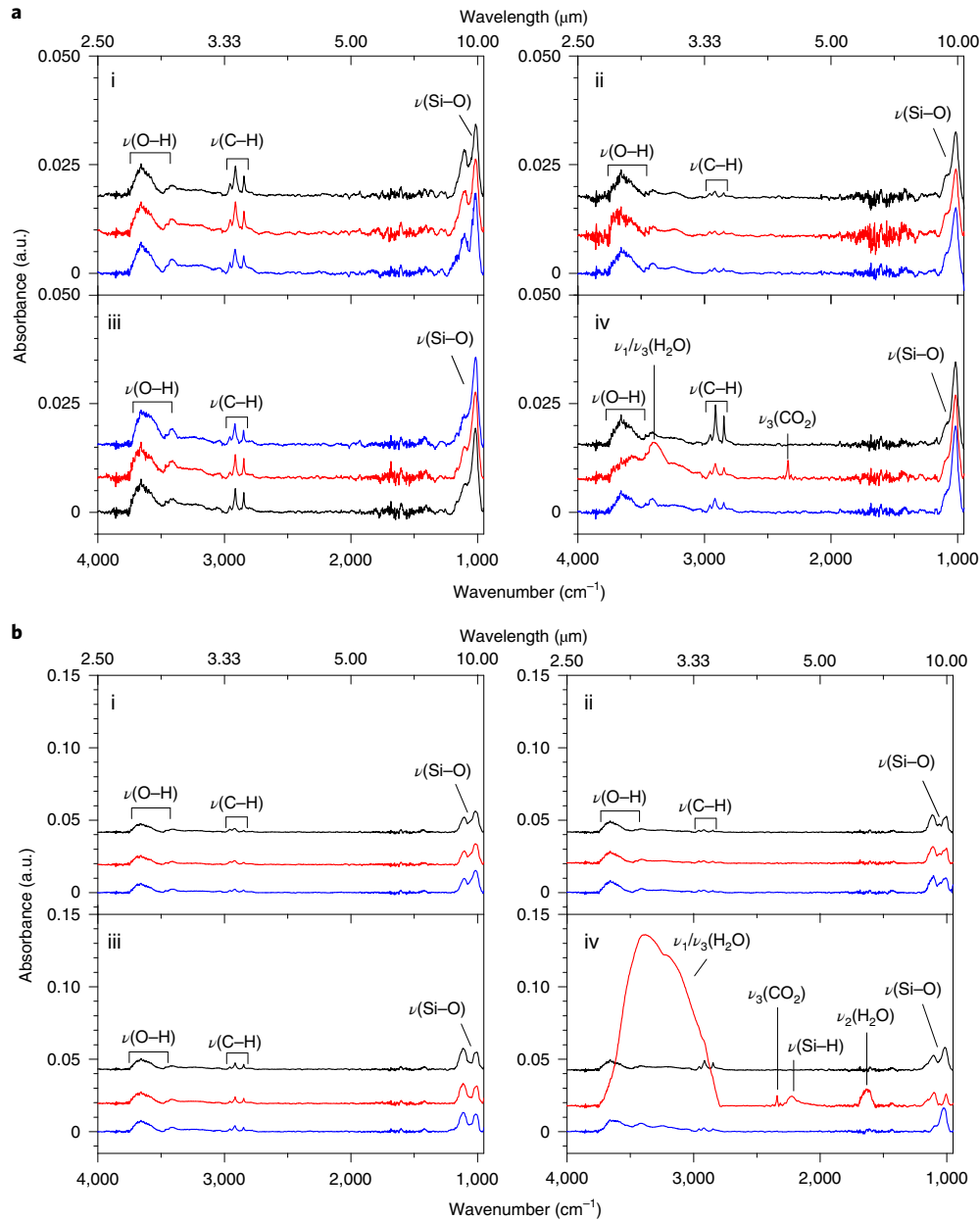


Fig. 1 | Infrared absorption spectra of the Murchison meteorite. a, b, Spectra taken before the irradiation, after the irradiation and after the completed TPD phase are coloured in black, red and blue, respectively. Infrared spectra were acquired for four separate irradiations: blank (top left), electron exposure (top right), carbon dioxide laser exposure (bottom left) and electron and carbon dioxide laser exposure (bottom right). Each experimental simulation was carried out at two temperatures: 5 K (**a**) and 150 K (**b**). All spectra are baseline corrected.

The shifts of the Si–O peaks are probably due to a phase change of the silicates¹⁴.

Having analysed the evolution of the organics, water and carbon dioxide via infrared spectroscopy, it is central to relate these findings to the mass spectroscopic analysis of the samples during the exposure to radiation and the TPD phase. During the irradiation phase, no radiation-generated products are released from the minerals into the gas phase, which suggests that the newly formed molecules either remained within the minerals or existed on the surface as ice, for example, as the water and carbon dioxide ices detected using FTIR spectrometry (Fig. 1). However, during the TPD phase, the samples exposed to simultaneous charged-particle irradiation and heating via energetic-pulse-laser irradiation release water and carbon dioxide, as detected in the gas phase via their molecular

parent ions at $m/z=18$ (H_2O^+) and $m/z=44$ (CO_2^+) (Fig. 3), where m/z is the mass-to-charge ratio.

For the sample that was dual irradiated at 5 K, the TPD profile of CO_2 depicts three maxima, while two peaks are observed for water (Fig. 3). The three desorption peaks in the range of 82–110 K, 135–165 K and 172–235 K are attributed to separate CO_2 desorption, molecular volcano desorption of CO_2 as a result of the phase change of water¹⁵, and co-desorption of the trapped CO_2 with water, respectively¹⁶. The temperature ranges are 15–20 K higher than those of the pure binary CO_2 and water ices, which is probably due to the molecular interaction between the water and carbon dioxide and between the water and carbon dioxide and silicates. The co-desorption of CO_2 with water (160–235 K; Fig. 3) is also observed in the TPD phase of the sample irradiated at high temperature. It should

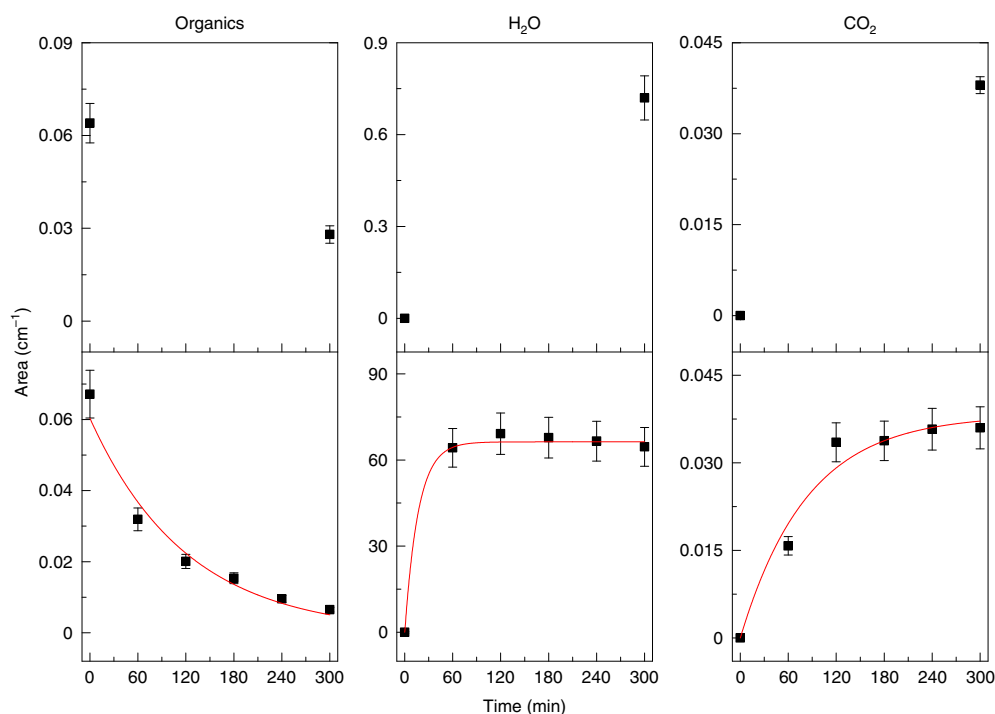
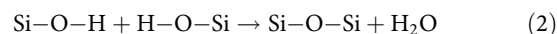
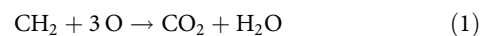


Fig. 2 | Temporal evolution and kinetic fits. Temporal profiles of the integrated areas of the infrared bands of the C–H stretching mode (left), water (middle) and carbon dioxide (right) during the dual irradiation exposure of the Murchison sample at 5 K (top) and 150 K (bottom). The first-order kinetic fits are overlaid as red curves. The error bars are $\pm 10\%$ of the corresponding areas.

be highlighted that an irradiation of the Murchison samples with only energetic electrons or the laser does not reveal any noteworthy ion counts of subliming molecules. These findings are consistent with the results of the infrared spectroscopic analysis, which show that only a simultaneous space weathering of the Murchison samples with proxies for charged particle and micrometeorite impact bombardment lead to the degradation of organics and concurrent formation of carbon dioxide and water.

We attempt to explain the underlying degradation and formation mechanisms. The interaction of energetic electrons with silicates like phyllosilicates in the Murchison meteorite generates suprathreshold oxygen atoms, which in turn efficiently oxidize any organics within the sample. Since the oxygen atoms have excess kinetic energy, the oxidation operates even at temperatures as low as 5 K and leads to the formation of water and carbon dioxide, which occurs through the reaction of the oxygen atoms with the hydrogen and carbon atoms of the organics. This reaction transpires over the typical penetration depth of the energetic electrons, $0.14\ \mu\text{m}$ (Supplementary Fig. 1 and Supplementary Table 2). In the Murchison meteorite, the organics represent a complex mixture, and their infrared identification is based on the CH_2 and CH_3 stretching modes. Considering a hydrogen-to-carbon ratio of the organics in the Murchison meteorite of $\text{H}/\text{C} \approx 2$ (ref. ¹⁷), the oxidation of each CH_2 moiety generates one carbon dioxide molecule and one water molecule (equation (1)). Quantitatively, the oxidation should only result in the formation of $(1.9 \pm 0.4) \times 10^{14}$ H_2O , which is equal to the amount of the CO_2 molecules detected by mass spectrometry (Supplementary Table 3). Once formed within the minerals, the intense pulsed-laser irradiation might induce thermal diffusion of the water and carbon dioxide molecules to the surface, where they can be detected via infrared spectroscopy and from where these species may sublime during the TPD phase. Furthermore, the simulated micrometeorite impact can ‘pre-damage’ or vibrationally excite the Si–O stretches in those mineral layers, which are simultaneously exposed to the energetic electrons. Here, vibrationally excited molecules have been

revealed to undergo more efficient bond cleavage processes and reactions compared to their counterparts in the vibrational ground state¹⁸. This in turn may result in an enhanced production of energetic oxygen atoms, which are available for the oxidation process. However, considering that $(1.9 \pm 0.4) \times 10^{14}$ carbon dioxide and $(2.0 \pm 0.4) \times 10^{15}$ water molecules were formed during the combined irradiation (Supplementary Table 3), the low-temperature oxidation of the organics can contribute at most 10% of the total water production. Therefore, a second source of water has to exist. Here, dehydration of the hydroxyl bonds may contribute to the formation of water in the present experiments. Formally, this can be expressed as in equation (2), which represents a condensation of two hydroxyl groups under elimination of water and the formation of a Si–O–Si moiety¹⁹. The fact that these processes do not operate when the samples are exposed to laser heating alone suggests that prior bond ruptures induced by energetic electrons might be essential to initiate the condensation reactions.



It should be mentioned that since the infrared absorption coefficient of the O–H stretching mode varies by around two orders of magnitude in different matrix environments²⁰, comparison of the O–H peak areas of water and phyllosilicates is impracticable for verifying the reaction in equation (2). However, an obvious change in the Si–O peak is observed upon dual irradiation of the sample at 150 K (Fig. 1), which endorses the reaction in equation (2).

The existence of two mechanisms for generating water on the surfaces of the samples is also supported by the extracted rate constants from the high-temperature irradiation experiment (Fig. 2b). Here, the rate constant of the decay of the organics, via equation (1), of $(1.4 \pm 0.2) \times 10^{-4}\ \text{s}^{-1}$ agrees well, within the error limits, with the rate constant linked to the carbon dioxide rise profile of

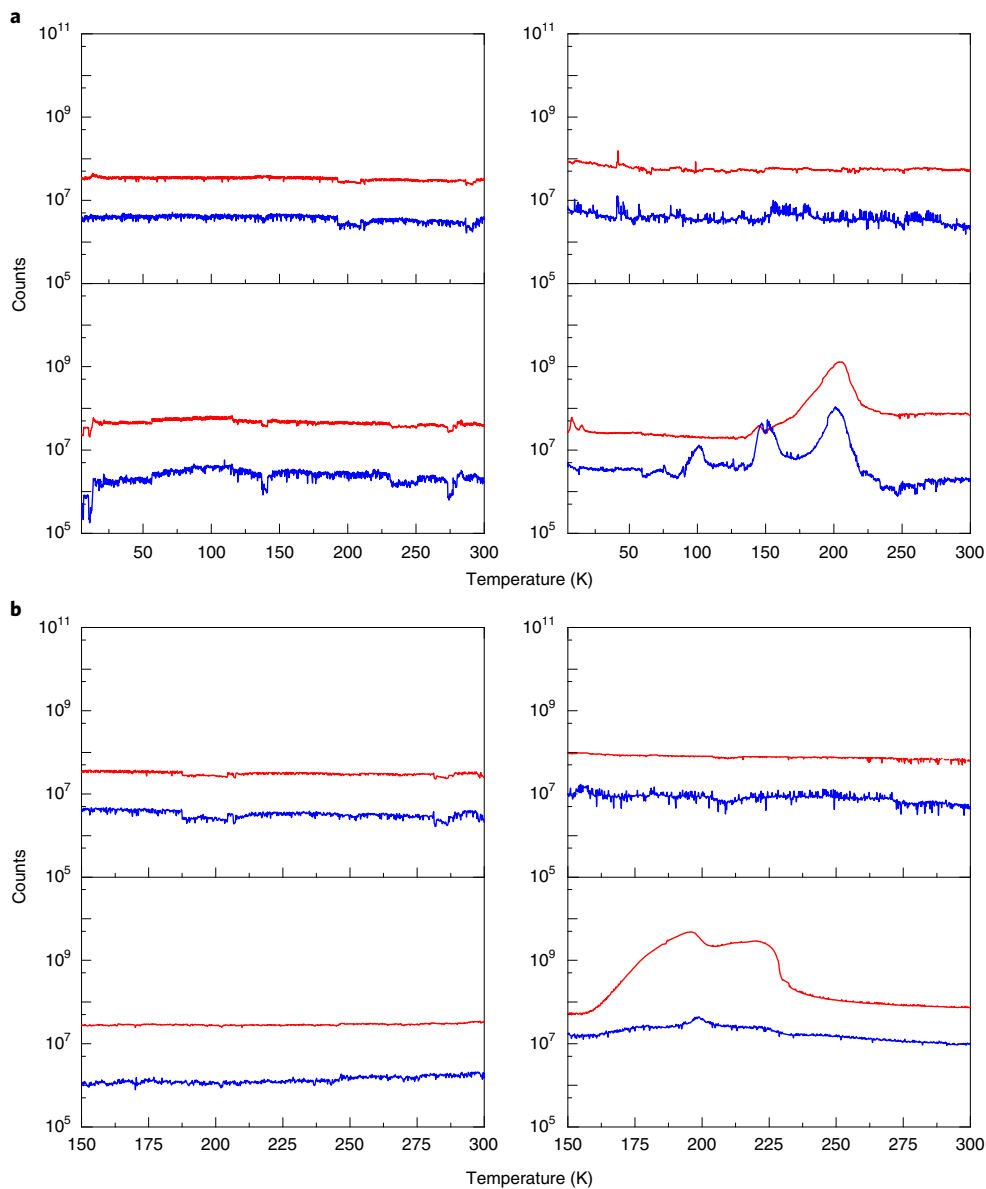


Fig. 3 | Quadrupole mass spectrometry profiles recorded during TPD. a,b, Data for $m/z=18$ (H_2O^+ ; red) and 44 (CO_2^+ ; blue) are shown. QMS data for four separate irradiations are displayed: blank (top left), electron exposure (top right), carbon dioxide laser exposure (bottom left) and electron and carbon dioxide laser exposure (bottom right). Irradiations were performed at 5 K (**a**) and 150 K (**b**).

$(2.0 \pm 0.5) \times 10^{-4} \text{ s}^{-1}$. If water is only formed via the oxidation of the organics, a rate constant for water formation of this magnitude is expected. However, the extracted rate constant is $(9.8 \pm 1.4) \times 10^{-4} \text{ s}^{-1}$, which is a factor of about five higher than predicted by equation (1). This discrepancy can only be explained through the existence of a second water-forming mechanism such as the reaction in equation (2). Furthermore, there are only two hydrogen sources in the sample: organics and hydroxyl groups. More efficient generation of water during irradiation at 150 K than 5 K is probably due to a greater thermal diffusion effect and the existence of more vibrationally excited molecules at high temperature.

The energetic electrons used in this study only simulate the secondary electrons generated by the solar wind and galactic cosmic ray particles—primarily protons—penetrating the surfaces of asteroids. Whether these protons can react directly with the silicates on airless bodies, including the Moon, to generate water is a research frontier as well. Analysis of lunar samples^{21,22} and interplanetary dust particles²³ revealed that the exposure of silicates to solar-wind proton

irradiation may form H_2O and OH. However, detailed isotopic analysis indicates that the chemical composition in the lunar samples^{21,22} was modified by subsequent fractionation and/or admixed with other non-solar-wind sources. In addition, experiments using protons have yielded a wide range of results. Experiments conducted under high-vacuum conditions between 10^{-8} and 10^{-6} torr detected only OH signals²⁴ or H_2O (ref. ²⁵). Studies conducted under UHV conditions (10^{-10} to 10^{-9} torr) yielded inconsistent results as well^{23,26,27}. In the present study, we have shown that non-reactive electrons coupled with intense thermal shock could generate water by low-temperature oxidation of organics and mineral dehydration without the need for proton irradiation. Although further work is needed to untangle the details of the underlying reaction mechanisms on the microscopic level and quantify the contribution of these mechanisms to the surface water on asteroids compared to other proposed sources such as subsurface reservoirs¹ and shock-induced dehydration²⁸, our findings still clearly reveal the necessity of cumulative effects and coordinated exposure of minerals to distinct

components of space weathering, and help to rationalize the spectroscopic signatures of water and hydroxyl radicals as detected on airless bodies and to decipher the contemporary distribution of water in our Solar System.

Methods

Simulation experiments. The experiments were conducted in a contamination-free UHV stainless-steel chamber evacuated to a few 10^{-11} torr by exploiting magnetically suspended turbomolecular pumps backed by an oil-free scroll pump¹⁰. Within the chamber, a silver mirror substrate is interfaced to a cold head cooled to 5.5 ± 0.1 K by a closed-cycle helium compressor (Sumitomo Heavy Industries, RDK-415E). A temperature of 150 K could be achieved by heating the sample using a cartridge heater. By utilizing a doubly differentially pumped rotational feedthrough (Thermionics Vacuum Products, RNN-600/FA/MCO) and an UHV-compatible bellow (McAllister, BLT106), the substrate can be rotated in the horizontal plane and translated in the vertical plane, respectively. Murchison meteorite powder (0.0306 ± 0.0005 g, grain size $< 45 \mu\text{m}$) was pressed onto the silver mirror. Taking into account the average density (2.83 ± 0.18 g cm⁻³) (ref. 29) and the area of the solid sample (1.9 ± 0.2 cm²), the average thickness of the samples was calculated to be $57 \pm 7 \mu\text{m}$. Each sample along with the entire chamber was baked to 333 K for several days. No surface contamination exists.

The infrared spectra of each sample was measured using a Nicolet 6700 FTIR spectrometer in the mid-infrared ($6,000$ to 400 cm⁻¹) range with 4 cm⁻¹ spectral resolution. Each sample was then cooled to 5.5 ± 0.1 or 150.0 ± 0.1 K, whereupon it was irradiated by either energetic electrons with an energy of 5 keV from a SPECS EQ 22-35 electron gun, by infrared radiation from a SYNRAD Firestar v40 5 kHz pulsed carbon dioxide laser (at 14% of full power) (Supplementary Fig. 2), or by both (Supplementary Tables 1 and 2). Energetic electron and infrared laser irradiation simulate secondary electrons created by the penetration of solar-wind ions and galactic cosmic rays into the asteroid and thermal effects of micrometeorite bombardments, respectively^{5,6,10,30,31}. The irradiation dose of the 5 keV electrons as calculated via Monte Carlo simulations (CASINO) and the energy deposited by the laser are compiled in Supplementary Table 2. The carbon dioxide laser can effectively melt minerals such as olivine to generate chondrule analogues³² and cause lattice disturbance³³; therefore the laser is able to simulate the thermal effects of micrometeorite impact. Researchers studying the effects of space weathering in the laboratory simulate micrometeorite impacts by infrared lasers with nanosecond^{30,34-36} and microsecond pulses³⁷⁻⁴³. The nanosecond laser experiments simulate the initial impact-induced shock heating, which results in projectile vapourization, whereas the microsecond laser experiments encompass the timescale of thermal dissipation to impact-adjacent regions, which eventually drives bond-breaking processes and hence the chemistry. The irradiated samples were kept at 5.5 ± 0.1 K or 150.0 ± 0.10 K for one hour and then warmed up to 300 K at a rate of 1 K min⁻¹. In situ FTIR spectra were collected before the irradiation, after the irradiation and after the TPD phase. In situ FTIR spectra were also collected in 60-min intervals during the dual irradiation at 150 K.

During all of the experiments, mass spectra of the species in the gas phase were recorded using an Extrel 5221 QMS operating in residual-gas-analyser mode with an electron impact ionization energy of 70 eV. Blank experiments were performed by conducting the same experimental sequence, but without irradiating the samples. The column densities of organics, CO₂ and H₂O in the sample before and after dual irradiation at 5 K and 150 K were calculated from infrared data (Supplementary Table 3). Since the Murchison meteorite contains a complicated mixture of organics, we calculated the column densities based on the C–H stretch absorption coefficients of several typical organic molecules^{12,44}. Since the IR absorption coefficients depend on the matrix environments²⁰, we calculate the column density ranges for these species based on their absorption coefficients from distinct experiments (Supplementary Table 3)^{12,20}. The amounts of the sublimed CO₂ and H₂O molecules during the TPD phase were also determined from the QMS data (Supplementary Table 3), which agree with the ranges extracted from the IR data.

Planetary context for experimental simulations. It is important to relate the laboratory simulations to the actual conditions in space. No single simulation experiment can reproduce the chemical complexity and diverse radiation environment of asteroids and airless bodies simultaneously. Real surfaces of airless bodies are exposed to a complex array of processes¹¹ that can be grouped into two broad categories: (1) irradiation by electromagnetic radiation or particles from the Sun and galactic sources, and (2) micrometeorite impacts. Hence, to gain a systematic understanding of the most fundamental processes that lead to the formation of water on airless bodies, we carried out simulation experiments with well-defined conditions.

Charged-particle irradiation. The particle component of the galactic cosmic radiation field consists of about 98% protons (H⁺) and 2% helium nuclei (He²⁺) and has an energy distribution maximum at about 10 MeV. These and higher-energy particles can easily penetrate silicates. For example, a 10 MeV cosmic-ray proton loses its energy almost exclusively (99.999%) via electronic interaction

with the target molecules. As a high-energy cosmic-ray particle penetrates a solid, it produces a primary ionization track perpendicular to the trajectory within which these electronic interaction processes primarily lead to bond ruptures and ionization of the molecules. During the ionization process, secondary electrons are released, leading to further bond-ruptures via inelastic energy-transfer processes. In our experiments, we simulate the effects of energetic charged particle implantation such as energetic protons exploiting energetic electrons as a proxy^{10,45-49}, which are generated as secondary electron cascades within the track of the primary implant once penetrating solid matter such as silicates. These processes contribute almost exclusively to the energy loss of the galactic cosmic rays⁵⁰⁻⁵³. The dose from the electrons generated by penetrating high-energy solar protons and galactic cosmic rays in the asteroid belt at a distance of 3 AU was determined to be 6.9×10^{-6} eV AMU⁻¹ yr⁻¹, which is one-ninth of the reported dose at a distance of 1 AU (6.2×10^{-5} eV AMU⁻¹ yr⁻¹) (ref. 54). Therefore, our energy dose is equivalent to those received by airless bodies in $> 10^6$ yr (Supplementary Table 2).

Laser irradiation. We simulate the thermal effects of micrometeorite impacts through infrared laser irradiation. The repetition rate, number of shots, energy per pulse and irradiation area of the laser are 5 kHz, 9×10^7 , 1.12 mJ and 0.7 ± 0.1 cm², respectively. Similar laser parameters (30 – 40 kHz, 0.6 – 1.2 mJ per pulse, ~ 0.1 mm diameter) have been used to simulate the thermal effect of micrometeorite impact^{37-43,55} and induced spectral similarity between ordinary chondrites and S-type asteroids. Our laser is milder as it was not focused, and replicates the heat pulses experienced within the target away from the immediate micrometeorite impact zone. While the energy of an individual impact into an asteroid in the asteroid belt is lower than for the Moon at 1 AU, the accumulated micrometeorite impact energy ($1,000$ J m⁻² yr⁻¹) due to a greater flux of micrometeoroids is about two orders of magnitude⁵⁶ higher than that on the Moon (10 J m⁻² yr⁻¹) (refs. 57,58) as the asteroid belt and Jupiter-family comets are the sources for the micrometeorites⁵⁹. Considering that the exact size distribution of the micrometeorites is unknown⁶⁰, care should be taken to quantitatively compare how the timescale in the laboratory relates to the actual exposure in the Solar System, and the simulated timescale of $> 10^6$ years is taken as an approximation³⁰. As shown in Fig. 2b, only a few seconds of irradiation, which corresponds to less than 10^5 yr, can generate water.

Laser penetration depth. The penetration depth δ of the laser is defined as the power the light has to decrease to reach $1/e$ of its value at the surface:

$$\delta = \frac{\lambda}{4\pi\kappa} \quad (3)$$

where λ is the wavelength of the light ($10.6 \mu\text{m}$) and κ is the imaginary part of the complex refractive index of the Murchison meteorite. The planetary science community adopted a κ value for Murchison similar to the κ value of the Tagish Lake meteorite for $10.6 \mu\text{m}$ light, that is $\kappa = 0.04$ (ref. 61). Using this value, δ is calculated to be $21 \mu\text{m}$.

Water-ice calibration. Water vapour was deposited through a glass capillary array to a silver mirror. A laser interferogram was obtained by reflecting a HeNe laser at $\lambda = 632.8$ nm (Melles Griot, 25-LHP-213) off the silver substrate. The incident angle of the laser is $\theta_1 = 4^\circ$ (ref. 62). Supplementary Fig. 3 shows the interference plot recorded during ice deposition. At the deposition stop time, $m = 2.05$ fringes had accumulated. Then the thickness of the ice d can be determined using the following:

$$d = \frac{m\lambda}{2\sqrt{n_{\text{H}_2\text{O}}^2 - \sin^2 \theta_1}} \quad (4)$$

where $n_{\text{H}_2\text{O}}$ is the refractive index of water. Using the reported¹² value of $n_{\text{H}_2\text{O}} = 1.27 \pm 0.02$, the ice was calculated to be 510 ± 10 nm thick.

Then an IR spectrum of the ice was recorded using a FTIR spectrometer (Nicolet 6700). The incident angle of the IR beam is $\theta_2 = 43^\circ$. Supplementary Fig. 4 depicts the O–H peaks of the ice. The absorption coefficient (A_{exp}) can be determined using:

$$A_{\text{exp}} = \frac{\ln(10)M \int_{\tilde{\nu}_1}^{\tilde{\nu}_2} A(\tilde{\nu})d(\tilde{\nu}) \sqrt{n_{\text{H}_2\text{O}}^2 - \sin^2 \theta_2}}{2N_A d \rho n_{\text{H}_2\text{O}}} \quad (5)$$

where $\int_{\tilde{\nu}_1}^{\tilde{\nu}_2} A(\tilde{\nu})d(\tilde{\nu})$ is the integrated peak area (measured in cm⁻¹), M is the molar mass of water (18 g mol⁻¹), ρ is the density of the water ice, $\tilde{\nu}$ is wavenumber (in cm⁻¹), and N_A is the Avogadro constant⁶². Using the reported¹² value of $\rho = 0.87 \pm 0.03$ g cm⁻³, A_{exp} was calculated with the present set-up to be $1.3 \pm 0.3 \times 10^{-16}$ cm molecule⁻¹, which is in good agreement with reported values¹² of 1 – 2×10^{-16} cm molecule⁻¹. It is important to note that equation (5) is only valid for ices thinner than $7 \mu\text{m}$ (ref. 63). For thicker ices, non-linear effects become substantial⁶³.

Timescales of micrometeorite impact on solid surfaces. We determined the timescales of the canonical two-stage crater formation for micrometeorite impact. The two stages of cratering are: (1) initial shock heating and (2)

subsequent thermal dissipation. Parameters considered in these calculations are micrometeorite size (r_g), micrometeorite density (ρ_g), impact velocity (v_0), target density (ρ_t) and an impact angle of 90° (straight on). These conditions establish the boundary conditions for the nearly spherical shock wave that is expected to penetrate the target and heat the target material.

Initial shock heating. Attenuation of shock wave in target. The initial radius and velocity of the shock wave in the target is given by r_s and v_s , respectively^{64–66}. The attenuation of a spherical shock's velocity in an ideal incompressible target as a function of the distance r away from the point of impact (for $r \geq r_g$) is given by:

$$v_s(r) \sim v_0 \left(\frac{r_g}{r} \right)^{3/2} \quad (6)$$

It is trivial to solve this equation for the position of the shock front (r_s) as a function of time by using the fact that $v_s = dr_s/dt$ to show that:

$$r_s(t) = r_g \left[1 + \frac{5}{2} \left(\frac{t}{t_0} \right) \right]^{2/5} \quad (7)$$

where $t_0 = \frac{r_g}{v_0}$ is the timescale for shock wave propagation into the projectile.

The impact of the projectile and resulting shock wave heats the target. With an equipartition between the kinetic energy and thermal energy, we determine the size of the target region that experiences substantial heating by determining the radius at which the shock wave velocity has decreased to a fraction f of the original shock wave velocity v_0 . Setting $v_s = f v_0$, the radius of this hemisphere that is substantially heated is given by:

$$r = \frac{r_g}{f^{2/3}} \quad (8)$$

Analytic determination of shock wave heating timescales. We temporarily defer discussion of the fraction f and focus on using this parameter to determine the minimum duration of impact-related target heating by setting $r_s = \frac{r_g}{f}$ in equation (7) and solving for the time t needed for the shock wave to grow to a size $\frac{r_g}{f}$. Solving for this shock heating characteristic time, we get:

$$t_{\text{shock}} = \frac{2}{5} t_0 (f^{-5/3} - 1) \quad (9)$$

Equation (9) can be used to determine the characteristic shock heating time as a function of micrometeorite size, velocity and f .

Threshold shock wave velocity for substantial heating. To determine the shock wave velocities that will result in substantial heating, we exploit the fact that the kinetic energy transferred to the target is converted to thermal energy instantly once it arrives. Thus, to determine the temperature of a region within the target, we equate the kinetic energy delivered by the shock per target molecule to an equivalent thermal energy, namely:

$$\frac{1}{2} m_{\text{SiO}_2} v_s^2 = 3 k_B T_s \quad (10)$$

where T_s is the temperature of the target region and k_B is the Boltzmann constant. Here, for simplicity, we have used the 'high-temperature' heat capacity of solids ($3k_B$) to determine this temperature. A more detailed treatment, treating the system as a Debye solid with temperature-dependent heat capacity, like that given in ref.⁶⁵, can be used to obtain a more accurate temperature determination, but we emphasize that this approach gives us a lower limit to the temperature increase. The local temperature T_s can be expressed as a function of the shock wave speed as:

$$T_s = 194 \left(\frac{v_s}{400 \text{ m s}^{-1}} \right)^2 \text{ K} \quad (11)$$

Thus, a shock wave velocity of approximately 400 m s^{-1} is needed to raise the average temperature of a target region by 194 K.

Timescale determination for shock heating of targets (method 1). To keep the discussion as general as possible, the timescales of crater heating for various dust grain projectile sizes (r_g), impact velocities and the critical shock wave velocity v_c (or equivalently $f = \frac{v_c}{v_0}$) are presented in Supplementary Fig. 5. Note that for dust grains larger than $10 \mu\text{m}$, the timescales for shock heating approach and exceed microseconds.

Timescale determination for shock heating of targets (method 2). A more conservative approach calculates the radius of the maximum volume heated by equating the available kinetic energy (half the kinetic energy of impact) with the thermal heat content change of a hemisphere of radius r_c heated to an average temperature⁶⁴. This condition is equal to:

$$\frac{1}{2} C_p \left(\frac{4}{3} \pi r_c^3 \right) \rho_t \Delta T_c = \frac{1}{2} \left(\frac{4}{3} \pi r_g^3 \right) \rho_g v_0^2 \quad (12)$$

where T_c is the average temperature of the crater, C_p is the heat capacity per unit mass of the target. Solving for r_c , it is easy to show that:

$$r_c = r_g \left(\frac{\rho_g}{\rho_t} \right)^{1/3} \left(\frac{v_0^2}{\Delta T_c C_p} \right)^{1/3} \quad (13)$$

which is given numerically by:

$$r_c = 1.12 \times r_g \left(\frac{v_0}{1 \text{ km s}^{-1}} \right)^{2/3} \left(\frac{700 \text{ J K}^{-1} \text{ kg}^{-1}}{C_p} \right)^{1/3} \left(\frac{500 \text{ K}}{\Delta T_c} \right)^{1/3} \quad (14)$$

Thus, an impact with a velocity of 1 km s^{-1} has enough kinetic energy to heat a region equal to its radius by about 500 K from the baseline temperature. Note that this condition is a relatively weak function of both the heat capacity assumed for the target as well as the change in temperature. The corresponding timescales for crater growth are plotted in Supplementary Fig. 6.

Timescale determination for shock heating of targets (method 3). Here we present a third method to determine the size of the region of direct shock heating using the condition that the target will cease to be compressed when the shock wave pressure is equal to the target material's strength (for example, crushing strength or ultimate compressive strength). This condition can be stated as:

$$P_{\text{crush}} \sim \rho_t v_s^2 \quad (15)$$

When taken together with the shock attenuation versus r relation (equation (6)), the crater radius is expected to be equal to:

$$r \sim r_g \left(\frac{\rho_t v_0^2}{P_{\text{crush}}} \right)^{1/3} \quad (16)$$

Note that this condition also correctly predicts the $v_0^{2/3}$ scaling for the radius of a crater as a function of velocity that is seen in the literature. Furthermore, this model correctly determines the r/r_g of micro-craters produced by $v \approx 6 \text{ km s}^{-1}$ glass projectile impacts in aluminum targets reported in ref.⁶⁷. Using this criterion for the final crater dimension, the expected crater growth and heating by direct-compression timescales are plotted in Supplementary Fig. 7. Note that these radii (and corresponding growth scales) are very similar to those shown in Supplementary Fig. 6.

Timescale determination for shock heating of targets (method 4). Numerical impact simulations using the iSALE-2D hydrocode⁶⁸ for a chondritic meteoroid (with an impactor mass range from 10^{-12} to 1 g) striking a chondritic non-porous target with a vertical impact speed of $1-10 \text{ km s}^{-1}$ suggested that the duration of the impact heating deposition into the target lasts from $10^{-4} \mu\text{s}$ for the smallest impactor size up to $10 \mu\text{s}$ for the largest impactor size. The investigated impact speed range can affect the energy transfer duration within one order of magnitude, for the same impactor size. There are two ways to determine the duration of the impact energy transfer. One way (1) is by observing the pressure wave traversing back into the projectile, marking the end phase of the energy partitioning between the target and the projectile when it reaches the back end of the projectile⁶⁴. This is a mathematical approximation derived from the Rankine–Hugoniot equation for planar shock waves and the energy partitioning during impact. The other way (2) is by considering the time until the projectile reaches the maximum temperature elevation, occurring during the contact and compression stages of cratering. The timescales between (1) and (2) mark the two end member values for the heat transfer during the earliest stages of impact: the contact and compression stages. Numerical simulations agree with the aforementioned methods.

Thermal dissipation. After a crater has stopped growing, there is still a significant amount of heat 'trapped' within the impactor and crater. The amount of time it takes for thermal dissipation, as we show here, is significant and is at least $1 \mu\text{s}$ for micrometeorites greater than $1 \mu\text{m}$ in radius. Following the approach reported in ref.⁶⁵, dimensional analysis of the thermal diffusion equation is used:

$$\frac{\partial T(r, t')}{\partial t} = D \nabla^2 T(r, t') \quad (17)$$

where the thermal diffusivity D of the target is given by:

$$D = \frac{K_T}{C_V} \quad (18)$$

and r is the radial coordinate, where $r=0$ is the location of the impact. t' is the amount of time elapsed since the region of the target with radius r_c was shock heated. C_V is the heat capacity of the shock-heated region per unit mass ($C_V = C_p \rho_t$) and K_T is the thermal conductivity. Using dimensional analysis of equation (17), it is trivial to see that the characteristic thermal dissipation timescale $t_{\text{dissipation}}$ is:

$$t_{\text{dissipation}} \sim \frac{r_c^2}{D} \quad (19)$$

Note that the characteristic thermal dissipation time of a spherical region that has been heated to a temperature larger than the surroundings is independent of the impact velocity, although higher impact velocities would be expected to achieve higher initial temperatures and larger craters.

Minimum thermal dissipation time. Taking the thermal properties of silicates, we determine the minimum thermal dissipation timescale by assuming that the minimum crater radius is equal to the size of the projectile ($r_c \approx r_g$). Assuming $C_p \approx 700 \text{ J K}^{-1} \text{ kg}^{-1}$, $\rho_i \approx 2,500 \text{ kg m}^{-3}$ and $K_T = 1.4 \text{ W m}^{-1} \text{ K}^{-1}$, yields a thermal diffusivity $D \approx 8 \times 10^{-7} \text{ m}^2 \text{ s}^{-1}$. This yields the following relationship between the minimum thermal dissipation time and projectile radius:

$$t_{\text{dissipation}} \sim 1.25 \left(\frac{r_c}{1 \mu\text{m}} \right)^2 \mu\text{s} \quad (20)$$

This thermal diffusion analysis alone strongly suggests that the duration of the heat pulse that results from micrometeorite impacts is at least $1 \mu\text{s}$ for micrometeorites $1 \mu\text{m}$ in diameter and increases dramatically for larger dust grains. Given that equation (20) is a characteristic time, the amount of time that the crater region sustains elevated temperatures will be significantly larger or multiples of $t_{\text{dissipation}}$.

Thermal dissipation time determination. More realistic determinations of the durations of heat pulses resulting from hypervelocity projectile impact can be calculated by setting r_c equal to either the radius of the impact crater (using methods 2 or 3) in combination with equation (20). The results of these calculations are shown in Supplementary Fig. 8.

In conclusion, our calculations show that for impactors with diameters from $1 \mu\text{m}$ to $10 \mu\text{m}$, indeed, the initial cratering with the thermal shock of micrometeorite impact lasts only 6 ns to 60 ns (Supplementary Figs. 6 and 7). However, the subsequent thermal dissipation times are calculated to last a few microseconds to a few hundred microseconds (Supplementary Fig. 8). Hence, calculated timescales are similar to the heating duration of our carbon dioxide laser.

Data availability

The data that support the plots within this paper and other findings of this study are available from the corresponding authors on reasonable request.

Code availability

The iSALE-2D hydrocode can be accessed at <https://isale-code.github.io/terms-of-use.html>

Received: 27 August 2018; Accepted: 27 August 2019;

Published online: 07 October 2019

References

- Campins, H. et al. Water ice and organics on the surface of the asteroid 24 Themis. *Nature* **464**, 1320–1321 (2010).
- Rivkin, A. S., Howell, E. S., Emery, J. P. & Sunshine, J. Evidence for OH or H₂O on the surface of 433 Eros and 1036 Ganymed. *Icarus* **304**, 74–82 (2017).
- Rivkin, A. S. & Emery, J. P. Detection of ice and organics on an asteroidal surface. *Nature* **464**, 1322–1323 (2010).
- Schorghofer, N. The lifetime of ice on main belt asteroids. *Astrophys. J.* **682**, 697–705 (2008).
- Gillis-Davis, J. J., Gasda, P. J., Bradley, J. P., Ishii, H. A. & Bussey, D. B. J. Laser space weathering of Allende (CV2) and Murchison (CM2) carbonaceous chondrites. In *46th Lunar and Planetary Science Conference 1607* (Lunar and Planetary Institute, 2015).
- Matsuoka, M. et al. Pulse-laser irradiation experiments of Murchison CM2 chondrite for reproducing space weathering on C-type asteroids. *Icarus* **254**, 135–143 (2015).
- Lantz, C. et al. Ion irradiation of the Murchison meteorite: Visible to mid-infrared spectroscopic results. *Astron. Astrophys.* **577**, A41 (2015).
- Thompson, M. S. et al. Coordinated analysis of an experimentally space weathered carbonaceous chondrite. In *50th Lunar and Planetary Science Conference 2045* (Lunar and Planetary Institute, 2019).
- Coradini, A. et al. The surface composition and temperature of asteroid 21 Lutetia as observed by Rosetta/VIRTIS. *Science* **334**, 492–494 (2011).
- Abplanalp, M. J. et al. A study of interstellar aldehydes and enols as tracers of a cosmic ray-driven nonequilibrium synthesis of complex organic molecules. *Proc. Natl Acad. Sci. USA* **113**, 7727–7732 (2016).
- Brunetto, R., Loeffler, M. J., Nesvorný, D., Sasaki, S. & Strazzulla, G. in *Asteroids IV* 597–616 (Univ. Arizona Press, 2015).
- Bouilloud, M. et al. Bibliographic review and new measurements of the infrared band strengths of pure molecules at 25 K: H₂O, CO₂, CO, CH₄, NH₃, CH₃OH, HCOOH and H₂CO. *Mon. Not. R. Astron. Soc.* **451**, 2145–2160 (2015).
- Jamieson, C. S., Mebel, A. M. & Kaiser, R. I. Understanding the kinetics and dynamics of radiation-induced reaction pathways in carbon monoxide ice at 10 K. *Astrophys. J. Suppl. Ser.* **163**, 184–206 (2006).
- Petkova, V. & Yaneva, V. Thermal behavior and phase transformations of nanosized carbonate apatite (Syria). *J. Therm. Anal. Calorim.* **99**, 179–189 (2010).
- Smith, R. S., Huang, C., Wong, E. K. L. & Kay, B. D. The molecular volcano: abrupt CCl₄ desorption driven by the crystallization of amorphous solid water. *Phys. Rev. Lett.* **79**, 909–912 (1997).
- Collings, M. P. et al. A laboratory survey of the thermal desorption of astrophysically relevant molecules. *Mon. Not. R. Astron. Soc.* **354**, 1133–1140 (2004).
- Schmitt-Kopplin, P. et al. High molecular diversity of extraterrestrial organic matter in Murchison meteorite revealed 40 years after its fall. *Proc. Natl Acad. Sci. USA* **107**, 2763–2768 (2010).
- Palma, J., Echave, J. & Clary, D. C. The effect of the symmetric and asymmetric stretching vibrations on the CH₃D + O(¹P) → CH₃ + OD reaction. *Chem. Phys. Lett.* **363**, 529–533 (2002).
- Roskosz, M. et al. Kinetic D/H fractionation during hydration and dehydration of silicate glasses, melts and nominally anhydrous minerals. *Geochim. Cosmochim. Acta* **233**, 14–32 (2018).
- Bennett, C. J., Ennis, C. P. & Kaiser, R. I. Experimental studies on the formation of D₂O and D₂O₂ by implantation of energetic D⁺ ions into oxygen ices. *Astrophys. J.* **782**, 63 (2014).
- Greenwood, J. P. et al. Hydrogen isotope ratios in lunar rocks indicate delivery of cometary water to the Moon. *Nat. Geosci.* **4**, 79–82 (2011).
- Liu, Y. et al. Direct measurement of hydroxyl in the lunar regolith and the origin of lunar surface water. *Nat. Geosci.* **5**, 779–782 (2012).
- Bradley, J. P. et al. Detection of solar wind-produced water in irradiated rims on silicate minerals. *Proc. Natl Acad. Sci. USA* **111**, 1732–1735 (2014).
- Ichimura, A. S., Zent, A. P., Quinn, R. C., Sanchez, M. R. & Taylor, L. A. Hydroxyl (OH) production on airless planetary bodies: evidence from H⁺/D⁺ ion-beam experiments. *Earth Planet. Sci. Lett.* **345–348**, 90–94 (2012).
- Managadze, G. G., Cherepin, V. T., Shkuratov, Y. G., Kolesnik, V. N. & Chumikov, A. E. Simulating OH/H₂O formation by solar wind at the lunar surface. *Icarus* **215**, 449–451 (2011).
- Burke, D. J. et al. Solar wind contribution to surficial lunar water: laboratory investigations. *Icarus* **211**, 1082–1088 (2011).
- Zhu, C. et al. Untangling the formation and liberation of water in the lunar regolith. *Proc. Natl Acad. Sci. USA* **116**, 11165–11170 (2019).
- Morlok, A., Koike, C., Tomioka, N., Mann, I. & Tomeoka, K. Mid-infrared spectra of the shocked Murchison CM chondrite: comparison with astronomical observations of dust in debris disks. *Icarus* **207**, 45–53 (2010).
- McCausland, P. J. A., Samson, C. & McLeod, T. Determination of bulk density for small meteorite fragments via visible light 3D laser imaging. *Meteorit. Planet. Sci.* **46**, 1097–1109 (2011).
- Sasaki, S., Nakamura, K., Hamabe, Y., Kurahashi, E. & Hiroi, T. Production of iron nanoparticles by laser irradiation in a simulation of lunar-like space weathering. *Nature* **410**, 555–557 (2001).
- Lantz, C. et al. Ion irradiation of carbonaceous chondrites: A new view of space weathering on primitive asteroids. *Icarus* **285**, 43–57 (2017).
- Cervantes-de la Cruz, K. E. et al. Experimental chondrules by melting samples of olivine, clays and carbon with a CO₂ laser. *Bol. Soc. Geol. Mex.* **67**, 401–412 (2015).
- Kissel, J. & Krueger, F. R. Ion formation by impact of fast dust particles and comparison with related techniques. *Appl. Phys.* **A** **42**, 69–85 (1987).
- Hiroi, T. & Sasaki, S. Importance of space weathering simulation products in compositional modeling of asteroids: 349 Dembowska and 446 Aeternitas as examples. *Meteorit. Planet. Sci.* **36**, 1587–1596 (2001).
- Brunetto, R., Roush, T. L., Marra, A. C. & Orofino, V. Optical characterization of laser ablated silicates. *Icarus* **191**, 381–393 (2007).
- Gillis-Davis, J. J. et al. Incremental laser space weathering of Allende reveals non-lunar like space weathering effects. *Icarus* **286**, 1–14 (2017).
- Moroz, L. V., Fisenko, A. V., Semjonova, L. F., Pieters, C. M. & Korotaeva, N. N. Optical effects of regolith processes on S-asteroids as simulated by laser shots on ordinary chondrite and other mafic materials. *Icarus* **122**, 366–382 (1996).
- Wasson, J. T., Pieters, C. M., Fisenko, A. V., Semjonova, L. F. & Warren, P. H. Simulation of space weathering of eucrites by laser impulse irradiation. In *29th Lunar and Planetary Science Conference 1940* (Lunar and Planetary Institute, 1998).
- Basilevsky, A. T. et al. Simulation of impact melting effect on spectral properties of Martian surface: implications for polar deposits. *Geochem. Int.* **38**, 390–403 (2000).
- Hiroi, T., Moroz, L. V., Shingareva, T. V., Basilevsky, A. T. & Pieters, C. M. Effects of microsecond pulse laser irradiation on Vis-NIR reflectance spectrum of carbonaceous chondrite simulant: implications for martian moons and primitive asteroids. In *34th Lunar and Planetary Science Conference 1324* (Lunar and Planetary Institute, 2003).

41. Moroz, L. V. et al. Reflectance spectra of CM2 chondrite Mighei irradiated with pulsed laser and implications for low-albedo asteroids and Martian moons. In *35th Lunar and Planetary Science Conference 1279* (Lunar and Planetary Institute, 2004).
42. Shingareva, T. V., Basilevsky, A. T., Fisenko, A. V., Semjonova, L. F. & Korotaeva, N. N. Mineralogy and petrology of laser irradiated carbonaceous chondrite Mighei. In *35th Lunar and Planetary Science Conference 1137* (Lunar and Planetary Institute, 2004).
43. Moroz, L. V. et al. Spectral properties of simulated impact glasses produced from martian soil analogue JSC Mars-1. *Icarus* **202**, 336–353 (2009).
44. Hudson, R. L., Gerakines, P. A. & Moore, M. H. Infrared spectra and optical constants of astronomical ices: II. Ethane and ethylene. *Icarus* **243**, 148–157 (2014).
45. Harris, T. D., Lee, D. H., Blumberg, M. Q. & Arumainayagam, C. R. Electron-induced reactions in methanol ultrathin films studied by temperature-programmed desorption: a useful method to study radiation chemistry. *J. Phys. Chem.* **99**, 9530–9535 (1995).
46. Boyer, M. C. et al. Dynamics of dissociative electron-molecule interactions in condensed methanol. *J. Phys. Chem. C* **118**, 22592–22600 (2014).
47. Boamah, M. D. et al. Low-energy electron-induced chemistry of condensed methanol: implications for the interstellar synthesis of prebiotic molecules. *Faraday Discuss.* **168**, 249–266 (2014).
48. Turner, A. M. et al. An interstellar synthesis of phosphorus oxoacids. *Nat. Commun.* **9**, 3851 (2018).
49. Shingledecker, C. N. & Herbst, E. A general method for the inclusion of radiation chemistry in astrochemical models. *Phys. Chem. Chem. Phys.* **20**, 5359–5367 (2018).
50. Bennett, C. J., Jamieson, C. S., Osamura, Y. & Kaiser, R. I. A combined experimental and computational investigation on the synthesis of acetaldehyde [CH₃CHO (X¹A')] in interstellar ices. *Astrophys. J.* **624**, 1097–1115 (2005).
51. Arumainayagam, C. R., Lee, H.-L., Nelson, R. B., Haines, D. R. & Gunawardane, R. P. Low-energy electron-induced reactions in condensed matter. *Surf. Sci. Rep.* **65**, 1–44 (2010).
52. Alizadeh, E., Orlando, T. M. & Sanche, L. Biomolecular damage induced by ionizing radiation: the direct and indirect effects of low-energy electrons on DNA. *Annu. Rev. Phys. Chem.* **66**, 379–398 (2015).
53. Boyer, M. C., Rivas, N., Tran, A. A., Verish, C. A. & Arumainayagam, C. R. The role of low-energy (≤ 20 eV) electrons in astrochemistry. *Surf. Sci.* **652**, 26–32 (2016).
54. Strazzulla, G. & Johnson, R. E. Irradiation effects on comets and cometary debris. In *International Astronomical Union Colloquium 243–275* (Cambridge Univ. Press, 1989).
55. Wasson, J. T. et al. Simulation of space weathering of HED meteorites by laser impulse irradiation. In *28th Lunar and Planetary Science Conference 1730* (Lunar and Planetary Institute, 1997).
56. Chapman, C. R., Paolicchi, P., Zappala, V., Binzel, R. P. & Bell, J. F. In *Asteroids II* 386–415 (Univ. Arizona Press, 1989).
57. Lucey, P. et al. Understanding the lunar surface and space-Moon interactions. *Rev. Mineral. Geochem.* **60**, 83–219 (2006).
58. Love, S. G. & Brownlee, D. E. A direct measurement of the terrestrial mass accretion rate of cosmic dust. *Science* **262**, 550–553 (1993).
59. Liou, J.-C. & Zook, H. A. Signatures of the giant planets imprinted on the Edgeworth-Kuiper belt dust disk. *Astron. J.* **118**, 580–590 (1999).
60. Grün, E., Zook, H. A., Fechtig, H. & Giese, R. H. Collisional balance of the meteoritic complex. *Icarus* **62**, 244–272 (1985).
61. Roush, T. L. Estimated optical constants of the Tagish Lake meteorite. *Meteorit. Planet. Sci.* **38**, 419–426 (2003).
62. Turner, A. M. et al. A photoionization mass spectroscopic study on the formation of phosphanes in low temperature phosphine ices. *Phys. Chem. Chem. Phys.* **17**, 27281–27291 (2015).
63. Gerakines, P. A., Bray, J. J., Davis, A. & Richey, C. R. The strengths of near-infrared absorption features relevant to interstellar and planetary ices. *Astrophys. J.* **620**, 1140–1150 (2005).
64. Melosh, H. J. *Impact Cratering: A Geologic Process* (Oxford Univ. Press, 1996).
65. Dominguez, G. Time evolution and temperatures of hypervelocity impact-generated tracks in aerogel. *Meteorit. Planet. Sci.* **44**, 1431–1443 (2009).
66. Zel'Dovich, Y. B. & Raizer, Y. P. *Physics of Shock Waves and High-Temperature Hydrodynamic Phenomena* (Courier Corporation, 2012).
67. Kearsley, A. T., Burchell, M. J., Hörz, F., Cole, M. J. & Schwandt, C. S. Laboratory simulation of impacts on aluminum foils of the Stardust spacecraft: Calibration of dust particle size from comet Wild-2. *Meteorit. Planet. Sci.* **41**, 167–180 (2006).
68. Prieur, N. C., Rolf, T., Wnnemann, K. & Werner, S. C. Formation of simple impact craters in layered targets: implications for lunar crater morphology and regolith thickness. *J. Geophys. Res. Planets* **123**, 1555–1578 (2018).

Acknowledgements

This work was supported by NASA under grant NNX16AO79G, awarded to R.I.K. and the University of Hawai'i at Mānoa. We also acknowledge the W. M. Keck Foundation for funding the construction of the surface-science machine. P. Crandall (University of Hawai'i at Mānoa, Department of Chemistry) provided advice to operate the charged-particle source and the laser. J.P. Bradley (University of Hawai'i at Mānoa, Hawai'i Institute of Geophysics and Planetology) provided advice on the thermal effects of the laser. G.D. acknowledges support by NSF grant 1616992.

Author contributions

R.I.K. and J.J.G.-D. designed the experiments. S.G., C.Z., M.J.A. and R.F. performed the experiments. G.D. and K.M. carried out the theoretical analyses. R.I.K., C.Z. and J.J.G.-D. wrote the manuscript, which was read, revised and approved by all co-authors.

Competing interests

The authors declare no competing interests.

Additional information

Supplementary information is available for this paper at <https://doi.org/10.1038/s41550-019-0900-2>.

Correspondence and requests for materials should be addressed to J.J.G.-D. or R.I.K.

Peer review information *Nature Astronomy* thanks Michelle Thompson and the other, anonymous, reviewer(s) for their contribution to the peer review of this work.

Reprints and permissions information is available at www.nature.com/reprints.

Publisher's note Springer Nature remains neutral with regard to jurisdictional claims in published maps and institutional affiliations.

© The Author(s), under exclusive licence to Springer Nature Limited 2019